Electronic coupling between graphene and topological insulator induced anomalous magnetotransport properties

Electronic Coupling between Graphene and Topological Insulator Induced Anomalous Magnetotransport Properties

Liang Zhang[1], Ben-Chuan Lin[1], Yan-Fei Wu[1], Hanchun Wu[2], Tsung-Wei Huang[3], Ching-Ray Chang[3], Xiaoxing Ke[4], Mert Kurttepeli[5], Gustaaf Van Tendeloo[5], Jun Xu[6], Dapeng Yu[1,7] & Zhi-Min Liao[1,8,*]

[1]State Key Laboratory for Mesoscopic Physics, School of Physics, Peking University, Beijing 100871, China

[2]School of Physics, Beijing Institute of Technology, Beijing, 100081, China

[3]Department of Physics, National Taiwan University, Taipei 10617, Taiwan

[4]Institute of Microstructures and Properties of Advanced Materials, Beijing University of Technology, Beijing 100124, China

[5]EMAT (Electron Microscopy for Materials Science), University of Antwerp, Groenenborgerlaan 171, B-2020 Antwerp, Belgium

[6]Electron Microscopy Laboratory, School of Physics, Peking University, Beijing 100871, China

[7]Department of Physics, South University of Science and Technology of China, Shenzhen 518055, China

[8]Collaborative Innovation Center of Quantum Matter, Beijing 100871, China

* E-mail: liaozm@pku.edu.cn.

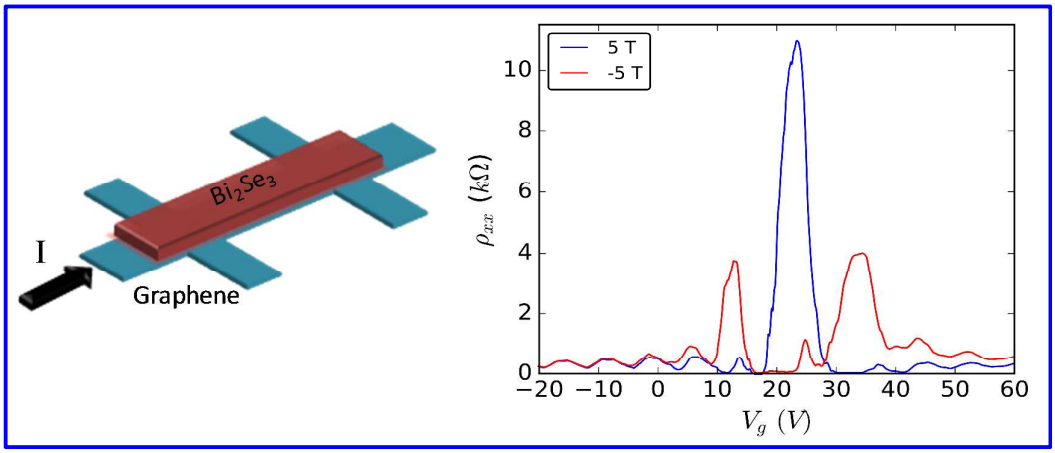

ABSTRACT: It has been theoretically proposed that the spin textures of surface states in a topological insulator can be directly transferred to graphene by means of the proximity effect, which is very important for realizing the two-dimensional topological insulator based on graphene. Here we report the anomalous

magnetotransport properties of graphene-topological insulator Bi_2Se_3 heterojunctions, which are sensitive to the electronic coupling between graphene and the topological surface state. The coupling between the p_z orbitals of graphene and the p orbitals of the surface states on the Bi_2Se_3 bottom surface can be enhanced by applying a perpendicular negative magnetic field, resulting in a giant negative magnetoresistance at the Dirac point up to about -91%. Obvious resistances dip in the transfer curve at the Dirac point is also observed in the hybrid devices, which is consistent with theoretical predictions of the distorted Dirac bands with nontrivial spin textures inherited from the Bi_2Se_3 surface states.

KEYWORDS: topological insulator, electronic coupling, proximity effect, negative magnetoresistance, asymmetric magnetoresistance

Graphene and surface states of topological insulators (TIs) can be described by two-dimensional (2D) massless Dirac Hamiltonian at the low energy excitations, which can be further modulated by adatoms adsorption or hybridization with other functional materials.[1-17] Owing to the high carrier mobility and intrinsic spin textures, TIs and graphene are promising for high speed electronics and spintronics.[18] Recent theories[9-13] have predicted that the hybridization between graphene and TIs can create nontrivial spin textures in graphene, even leading to quantum spin Hall states, i.e., 2D topological phases.[1] Generally, a rigorous $\sqrt{3} \times \sqrt{3}$ supercell of graphene stacked with TI is adopted in the calculations.[9-13] For an incommensurate graphene-TI

stacking, Zhang *et al.* suggested that the renormalized bands of the hybrid graphene can still acquire the spin textures from the surface states of the TI, even in the presence of surface roughness at the heterointerface.[12] The coupling between graphene and TI has been pursued *via* the angle resolved photoemission spectroscopy (ARPES). [19] On the other hand, the proximity effect has been demonstrated in both graphene and TI based hybrid devices, such as graphene/WS_2 (refs 6-8), graphene/$BiFeO_3$ (ref. 20), graphene/EuS (ref. 21) and Bi/$TlBiSe_2$ heterostructures.[22] Graphene-TI heterostructures have been fabricated to demonstrate the robustness of the topological surface state of Bi_2Se_3 (ref. 23), the 2D density of states (DOS) related tunneling process[24,25] and the current-induced spin polarization;[26] however, the proximity effect induced fascinating properties of graphene-TI hybrid devices are still unrevealed, which mainly affects the electronic properties of graphene in the vicinity of the Dirac point.[9-13] The strong hybridization will lead to a nonlinear dispersion relationship near the charge neutrality point, resulting in the enhancement of the DOS at the Dirac point in graphene.[12,13] Here, we report on the anomalous magnetotransport properties at the Dirac point in graphene coupled to Bi_2Se_3 nanoribbons.

RESULTS AND DISCUSSION

High quality Bi_2Se_3 nanoribbons grown by the chemical vapor deposition (CVD) method were transferred onto mechanically exfoliated monolayer graphene sheets on 285 nm SiO_2/Si substrates (see Figure S1 for details). The schematic diagram of the

patterned Hall bar device is shown in Figure 1a. The two current leads and four voltage probes for Hall measurements are Au/Pd (80 nm/5 nm) electrodes on graphene. A scanning electron microscopy (SEM) image of a typical graphene-Bi_2Se_3 device is presented in Figure 1b. The Bi_2Se_3 nanoribbon covers the entire transport channel of graphene with the same width. The back gate voltage V_g was used to tune the carrier density of graphene. The band structures of graphene and Bi_2Se_3 are also illustrated in Figure 1a. The Bi_2Se_3 nanoribbons used here are single crystals and the Fermi level is ~350 meV above the Dirac point of the surfaces states as revealed by the ARPES experiment.[27,28] Such heavy doping in Bi_2Se_3 will lead to (i) an enhanced hybridization between graphene and TI, considering that the DOS of TI increases dramatically;[12] (ii) a significant hexagonal warping effect of the TI surface states,[29] which is directly responsible for the out-of-plane spin component up to 12% in Bi_2Se_3 (refs 30, 31). To reveal the hybrid graphene heterointerface, a high resolution transmission electron microscopy (HRTEM) image of a cross section from a typical graphene-Bi_2Se_3 sample is shown in Figure 1c (see Figure S2 for elemental maps of Bi, Se and C). A thin oxide layer with a thickness of approximately 1~2 nm is noticed to cover Bi_2Se_3, which is due to the natural oxidization of Bi_2Se_3 in the atmosphere.

Gate-tunable conductivity σ_{xx} of the hybrid device is shown in Figure 1d, reproducing the field effect of graphene. The position of the Dirac point has been adjusted to zero volt, *i.e.* $V_g^* \equiv V_g - V_D$, where V_D is the measured Dirac point in back gate voltage V_g and V_D = 25 V for the device presented in Figure 1d. The approximately linear dependence $\sigma_{xx}(V_g^*) \propto V_g^*$ away from the Dirac point indicates

the charged impurity scattering dominated transport.[32] The mobility $\mu = \sigma_{xx}/en$ exceeds 1.5 $\mathrm{m^2V^{-1}s^{-1}}$ near the Dirac point and is ~0.6 $\mathrm{m^2V^{-1}s^{-1}}$ away from the Dirac point for both electrons and holes, obtained from the Hall measurements. Although n-type doped Bi_2Se_3 has a large conductivity, the minimum conductivity $\sigma_{xx,\mathrm{min}}$ of the graphene-TI hybrid device still approaches $4e^2/h$, further excluding the direct electrical contribution from the upper Bi_2Se_3. This is because the current probes were solely contacted with graphene and the insulating oxide layer significantly weakened the parallel conduction from Bi_2Se_3 bulk, leading to the small electric field $\vec{\mathbf{E}}_{\mathrm{bulk}}$ in Bi_2Se_3 bulk, and the tiny current density $\vec{\mathrm{j}}_{\mathrm{bulk}}$ in Bi_2Se_3 bulk. Therefore, we reasonably neglect the influence of the conductivity of Bi_2Se_3 σ_{TI} and the drag conductivity σ_{d} ($\sigma_{\mathrm{d}}^2 \ll \sigma_{xx}\sigma_{\mathrm{TI}}$) near the Dirac point in the following discussions. According to the analytic transport theory for the electron-hole puddle landscape developed by Adam *et al.*,[33] the residual carrier density n^* is estimated to be ~ $6.6 \times 10^{10}\mathrm{cm^{-2}}$. Besides, the thermally activated carrier density is $n_{\mathrm{e}} = n_{\mathrm{h}} \approx 0.52(k_{\mathrm{B}}T/\hbar v_{\mathrm{F}})^2$ at the charge neutral point, where k_B is the Boltzmann's constant. At T = 1.4 K, $n_{\mathrm{e}} = n_{\mathrm{h}} \approx 1.75 \times 10^{6}\mathrm{cm^{-2}} \ll n^*$. Therefore, we only need to consider the electron-hole puddles induced by the long-range Coulomb scattering at the Dirac point in the low temperature regime.

To demonstrate the unusual properties of the graphene-Bi_2Se_3 heterointerface, the magnetotransport properties were systematically measured. Figure 2 shows the resistivity ρ_{xx} and ρ_{xy} as a function of the gate voltage V_{g}^* under various perpendicular magnetic fields at 1.4 K. The transfer curves in Figs. 2a,b are shifted

linearly proportional to the strength of the applied magnetic field for clarity. It is found that the magnetotransport is largely asymmetric as switching the magnetic field direction normal to the graphene plane (see Figure 3 for detailed comparisons). Notably, the longitudinal resistivity ρ_{xx} at the Dirac point is largely suppressed and even exhibits a dip under a low negative magnetic field. Although the resistivity peaks of the zeroth Landau level (LL) recover under high negative magnetic fields, the values are still obviously smaller than the values under positive magnetic fields.

Under the magnetic field perpendicular to the graphene plane, the half-filled LLs, such as $N = -3, -2, \pm 1$ can be clearly identified as ρ_{xx} peaks, and the positions represented by $V_{\mathrm{g}}^{*,\mathrm{p}}$ are denoted by red filled circles in Figure 2a,b. When the Fermi level locates exactly at each LL, the ρ_{xx} peak positions are at $V_{\mathrm{g}}^{*,\mathrm{p}} = 4e^2NB/hc_{\mathrm{g}}$, where c_{g} is the effective capacitance of the back gate.[14,15] For a fixed Landau index *N*, the position $V_{\mathrm{g}}^{*,\mathrm{p}}$ is linearly dependent on the magnetic field strength *B*, as shown by the dashed lines in Figs. 2a,b. The slopes of the linear fittings extracted from Figs. 2a,b follow a linear relationship with the Landau index *N*, as shown in Figure 2c. The results indicate that the degeneracy of high-order LL structures ($|\mathrm{N}| > 0$) is maintained in the hybrid graphene devices under high magnetic fields, and the Dirac nature is further confirmed by the quantized Hall resistivity ρ_{xy} plateaus at $h/g(N + \frac{1}{2})e^2$ with $g = g_{\mathrm{s}}g_{\mathrm{v}} = 4$ in Figure 2d.

The evolutions of the $\rho_{xx}(V_{\mathrm{g}}^{*})$ and $\sigma_{xx}(V_{\mathrm{g}}^{*})$ curves near the Dirac point at various temperatures and under negative magnetic fields are shown in Figure 4a and Figure S3, respectively. The curves are shifted for clarity. The resistivities at the Dirac

point (ρ_{xx}^{D}) under different magnetic fields are extracted and shown in Figs. 4b,c. The $\rho_{xx}^{\mathrm{D}}(\vec{\mathrm{B}})$ is quite asymmetric between the positive and negative magnetic fields. By reversing the current direction, any mixture of the Hall signal origin is excluded for such asymmetry of the longitudinal resistivity (Figure 5). The asymmetric dependence of the longitudinal resistivity ρ_{xx} on the magnetic field *B* is consistent with the fact that the underlying graphene is only coupled to the bottom surface of Bi_2Se_3, where the direction of the external magnetic field will have distinct influences on the coupling strength. It is worth noting that there is a giant negative MR with magnitude of -91% under low negative magnetic field, as shown in Figure 4b. The negative MR is rather robust and still reaches -62.6% at 100 K, as shown in Figure 4c.

These anomalous magnetotransport properties cannot be explained by only considering the bare graphene or the graphene with a parallel conductive channel. Usually, the two-carrier model can be used to describe a zero-gap conductor with the same mobility μ for electrons and holes, giving $\rho_{xx}^{\mathrm{D}}(\mathrm{B}) = \rho_{xx}^{\mathrm{D}}(0)\frac{1+(\mu B)^2}{1+(\beta\mu B)^2}$, where $\beta = \frac{n_{\mathrm{e}}-n_{\mathrm{h}}}{n_{\mathrm{e}}+n_{\mathrm{h}}}$. Thus, at the charge-neutral point ($n_{\mathrm{e}} - n_{\mathrm{h}} \approx 0$), we have $\rho_{xx}^{\mathrm{D}}(\mathrm{B}) = \rho_{xx}^{\mathrm{D}}(0)[1 + (\mu B)^2]$ and $\rho_{xy} = 0$. Considering the spatial inhomogeneity of electron and hole with equal density and mobility, there is a positive magnetoresistance (MR) $\rho_{xx}^{\mathrm{D}}(\mathrm{B}) = \rho_{xx}^{\mathrm{D}}(0)[1 + (\mu B)^2]^{1/2}$.[34,35] If there is a small parallel conductivity σ^{p} due to the difference of density and mobility between electron and hole, the MR is modified as $\rho_{xx}^{\mathrm{D}}(B) = (\sigma_{xx}^{\mathrm{D}}(0)[1 + (\mu B)^2]^{-1/2} + \sigma^{\mathrm{p}})^{-1}$.[36] However, the above classic models cannot explain the MR behaviors in the graphene-Bi_2Se_3 hybrid devices.

We should realize that the hopping process between the p_z orbitals of carbon atoms in graphene and p orbitals of the bottom surface states in Bi_2Se_3 nanoribbons has significant influences on the transport properties in graphene near the Dirac point.[13] As predicted by theoretical models,[9-13] graphene can inherit spin-orbital textures from TI surface states near the Dirac point due to the electronic coupling. To understand the hybridization in the graphene-Bi_2Se_3 interface, the full low-energy effective Hamiltonian near the Dirac point $H_{\text{full}} = \begin{pmatrix} H_{\text{GG}} & H_{\text{GS}} \\ H_{\text{GS}}^{\dagger} & H_{\text{SS}} \end{pmatrix}$ can be adopted,[13] where the Hamiltonian of graphene H_{GG} is established on the basis states $\{|p_z, \text{n}\rangle, \text{n} = 1, \dots, 6\}$ of the six carbon atoms and basis transformation, H_{SS} describes the bottom surface states of topological insulator Bi_2Se_3 with basis states derived from $|p_{\pm}\rangle = \mp\frac{1}{\sqrt{2}}(|p_x\rangle \pm i|p_y\rangle)$ orbits of all Bi, Se atoms, and H_{GS} is the hybridization Hamiltonian between graphene and the TI bottom surface. The explicit matrix forms have been deduced in ref. 13, including key parameters of graphene and topological insulator, such as chemical potentials, Fermi velocities and hopping strengths. To further establish the effective Hamiltonian of the two gapless bands, the L*ö*wdin perturbation theory to the full Hamiltonian H_{full} is employed, and the effective Hamiltonian is described as

$$H_{\text{eff}}(k) = (C_2k^2 + C_3)\hat{z} \cdot (\vec{\sigma} \times \vec{k}) - \frac{C_1}{2}\left((k_x + ik_y)^3 + (k_x - ik_y)^3\right)\sigma_z + (\gamma_0 - C_0k^2)I_{2\times2}, \qquad (1)$$

where $\vec{\sigma} = (\sigma_x, \sigma_y, \sigma_z)$ are the Pauli matrices, $I_{2\times2}$ is identity matrix, and C_i $(i = 0,1,2,3)$ and γ_0 are the parameters that can be obtained by fitting the bands and are also related to the physical parameters of graphene and TI surface as

mentioned above. The detailed derivation in the framework of tight binding approximation can be found elsewhere (ref. 13). Note that the cubic spin-obit term of $H_{eff}(k)$ indicates the unusual properties of Dirac bands. Specifically, the C_0, C_1, and C_2 terms lead to the nonlinearity and the C_1 term indicates out-of-plane spin polarization. To understand the influences of graphene/TI coupling on the energy band, we explicitly plot Figure 6 to demonstrate how different terms affect the bands from Dirac-like linear band (only considering C_3, Figure 6a) to nonlinear band (considering C_3 and C_2, Figure 6b), and then to an oscillatory band structure if one takes into account of C_0 (Figure 6c).

The magnetic field interaction will certainly modify the full effective Hamiltonian $H_{\text{full}}(k)$, further altering the bands and the DOS near the Dirac point. However, the magnetic field effect on the full effective Hamiltonian $H_{\text{full}}(k)$ will result in the band alteration regardless of the sign of B. Further considering the hexagonal warping effect of TI surface states ($H_{\text{w}}^{\text{TIS}} = \lambda\left(\left(k_x' + ik_y'\right)^3 + \left(k_x' - ik_y'\right)^3\right)\sigma_z$) due to the n-type doping of Bi_2Se_3 bulk,[29] the cubic spin-orbit term of $H_{\text{eff}}(k)$ could be significant changed from the interaction among Graphene/TI and also external magnetic field, *i.e.*, $C_1^* = f(C_1, \lambda)$ is a function of C_1 and λ. The perpendicular magnetic field can interacted with the out-of-plane spin component $s_z \propto \langle\sigma_z\rangle$, which can be expressed as $H_{\text{Zeeman}}^{\perp} = g_{\perp} \cdot \vec{\sigma} \cdot \vec{B}_{\perp}$. Considering the asymmetric geometry at the graphene-TI interface, the positive and negative magnetic field will have asymmetric effects on the out-of-plane spin polarization of the surface states on TI, as shown in Figure 6d. To be specific, a negative magnetic field will

increase the out-of-plane spin polarization of the TI surface states and enhance the parameter C_1^*. With increasing the parameter C_1^*, the band nonlinearity and warping increases (Figure S4) as a result of the negative magnetic field enhanced graphene-TI electronic hybridization, leading to the resistivity dip in the transfer curves near the Dirac point and the negative MR of ρ_{xx}^{D}. Moreover, because the C_1^* term related bands are spin-polarized,[12,13] the inherited spin texture in graphene from the TI surface states may suppress the scatterings, and further decreases the resistivity.

The negative magnetic field induced enhancement of the graphene-TI coupling is further verified by the temperature dependence of the resistivity, as shown in Figure 7. Under zero magnetic field, ρ_{xx}^{D} decreases with increasing temperature, which could be attributed to the nonlinear energy bands of graphene coupled to the TI, because more carriers can be thermally activated to the multiple bands near the charge neutrality point.[12,13] Interestingly, the hybrid graphene exhibits metallic behavior under low negative magnetic fields (Figure 7). As discussed before, the negative magnetic field can enhance the conducting hybrid states in the graphene/Bi_2Se_3 heterointerface and may suppress the carrier back-scattering in graphene. The reduced thermal perturbation of the spin texture in graphene leads to a decrease of resistance with decreasing temperature.

We now turn to discuss the electronic coupling between graphene and topological surface state under high magnetic field. Under $|B| \geq 3$ T, the inset in Figure 4b shows that the $\rho_{xx}^{\mathrm{D}}(B > 0)$ and $\rho_{xx}^{\mathrm{D}}(B < 0)$ demonstrate the same dependence with B, where each data point of $\rho_{xx}^{\mathrm{D}}(B < 0)$ has been shifted up by 10 kΩ. The rapid

increase of ρ_{xx}^{D} under $|\mathrm{B}| \geq 3$ T at 1.4 K may be due to an energy gap Δ_g opening at $\mathrm{N} = 0$, as the experimental data shown in the inset in Figure 4b are well fitted by $\rho_{xx}^{\mathrm{D}} \propto \exp(\frac{B}{k_{\mathrm{B}}T})$ with $\Delta_g \propto$ B. The energy gap could be induced by Zeeman splitting $E_Z = \mathrm{g}\mu_{\mathrm{B}}B$ with g=2 and/or Coulomb interaction $E_C = \frac{e^2}{4\pi\varepsilon_0\varepsilon_r l_B}$, where μ_{B} is the Bohr magneton, $\varepsilon_r \approx 2.5$ is the effective dielectric constant and $l_B = \sqrt{\frac{\hbar}{eB}}$ is the magnetic length. Basically, Zeeman energy and the leading order of Coulomb interaction $\delta E_C = \frac{\mathrm{a}}{l_B} E_c$ has the same order given the field strength B, where a is the lattice constant. Therefore, we can't distinguish from the two origins here. Under 14 T, $E_Z \approx 19\,K$ and $\delta E_C \approx 20\,K$, which is consistent with the rapid rise of ρ_{xx}^{D} with decreasing temperature below 20 K shown in Figure 7b. At high temperatures, the small energy gap is less important and the MR can be described by $\rho_{xx}^{\mathrm{D}}(\mathrm{B}) = \rho_{xx}^{\mathrm{D}}(0)[1 + (\mu B)^2]^{1/2}$ for the graphene system at the Dirac point with a spatial inhomogeneity of electron-hole puddles, which is responsible for the observed linear relationship $\rho_{xx}^{\mathrm{D}} \propto B$ under $|B| > 3$ T at 100 K (Figure 4c). More detailed MR behaviors at different temperatures are presented in Figure S5.

The electronic coupling between graphene and topological surface state also has a notable influence on the quantum Hall effect. Distinct from individual graphene, the forward and backward propagating quantum Hall edge states in the hybrid graphene devices can interact with each other *via* the coupled Bi_2Se_3 nanoribbon. Specifically, the momentum relaxation *via* the Bi_2Se_3 bulk states makes the Hall conductivity deviate from the quantized values at the electron side, as shown in Figure 8. The scattering between graphene and Bi_2Se_3 bulk states is further clearly demonstrated by

directly contacting the voltage probes with both graphene and Bi_2Se_3 (see Figure S6). Under 14 T strong magnetic field, the zero Hall conductivity plateau emerges at Dirac point, as shown Figure 8, indicating the gapless bands are finally gapped that is consistent with the above discussion. Moreover, the renormalized bands in graphene coupled to TI will be largely weakened under intense magnetic field, as the time-reversal symmetry can be broken by the magnetic field.

The anomalous magnetotransport properties are rather common in our measured several graphene- Bi_2Se_3 samples. Moreover, in some samples, two Hall conductivity σ_{xy} plateaus quantized at $\pm e^2/h$ under an intermediate magnetic field 6 T can be clearly observed, as shown in Figure 9. The developing $\pm e^2/h$ Hall conductivity plateaus are ascribed to the partially lifted degeneracy of graphene,[12,13] which is consistent with the theoretical predication of the band structures. Specifically, the original fourfold degenerate Dirac bands distort into two nonlinear gapless bands with enhanced DOS near the Dirac point (Figure 6), and two Rashba-type gapped bands. Thus, one quantized conductance can be observed in the moderate magnetic field. Under strong field, *i.e.*, 14 T, the symmetry-broken will induce the appearance of the zero Hall plateau and the ruin of fine band structures, that is, the disappearance of the $\pm e^2/h$ Hall plateaus. It should be noted that the electronic coupling between graphene and Bi_2Se_3 is much sensitive to the thickness of the oxide layer outside Bi_2Se_3. Although appropriate insulating oxide layer should be necessary for the prevention of directly electric contact between graphene and TI, enhanced graphene-TI coupling is expected with further reducing the thickness of the oxide

layer. Nevertheless, it is very difficult for us to control the thickness of the oxide layer at the current stage. Further theoretical and experimental studies are necessary in future works.

CONCLUSIONS

In summary, we have demonstrated the electronic coupling induced anomalous MR in graphene-TI hybrid devices. The renormalized band structures of graphene result in a resistivity dip in the transfer curve near the Dirac point, which can be further enhanced by external negative magnetic field. Our observations should inspire more works to further understand the coupling between graphene and topological insulators, which are valuable to realize exotic topological states based on graphene hybrid devices.

METHODS

Device fabrication. The monolayer graphene was mechanically exfoliated from Kish graphite onto SiO_2/Si substrates and identified by Raman spectroscopy. Then the topological insulator Bi_2Se_3 nanoribbon grown by CVD method was directly transferred onto the top of the graphene sheet by a micromanipulator. A dry mechanical transfer method can avoid contamination at the graphene/Bi_2Se_3 interface. Standard electron-beam lithography and oxygen plasma etching were employed to shape the underlying graphene to a Hall bar. The fabrication processes are schematically illustrated in supplementary Figure S1. The width of the graphene Hall

bar was the same as that of the top Bi_2Se_3 nanoribbon. The Au/Pd (80 /5 nm) electrodes were only contacted with graphene, eliminating direct conduction contributions from the Bi_2Se_3 nanoribbon.

Transport measurements. The transport measurements were performed in an Oxford cryostat with a variable temperature insert and superconductor magnet. The temperature can be decreased to 1.4 K and the magnetic field can be swept up to 14 T. The electrical signals were measured using a low frequency lock-in technique with the bias current of 0.1 μA.

Band structure calculations. If $k_y = 0$, the Hamiltonian of Eq (1) can be simplified as $H_{\text{eff}}(k_x) = \begin{pmatrix} -C_1k_x^3 - C_0k_x^2 & i(C_2k_x^3 + C_3k_x) \\ -i(C_2k_x^3 + C_3k_x) & C_1k_x^3 - C_0k_x^2 \end{pmatrix}$. The eigenenergy $E(k_x) = -C_0k_x^2 \pm \sqrt{(C_1k_x^3)^2 + (C_2k_x^3 + C_3k_x)^2}$, thus if $C_0 = C_1 = C_2 = 0$, the spectra will be the linear bands in Figure 6a; when $C_0 = C_1 = 0$ and $C_2 \neq 0$, the bands will be in cubic dependence of k_x (in Figure 6b). When the $C_0 \neq 0$ and is larger than C_1 and C_2, the band becomes oscillatory near E=0 (in Figure 6c). In general, the energy spectra can be calculated directly from numerical solving the eigenenergy problem of Eq (1) which is $det[H_{\text{eff}} - E] = 0$ along any k direction. For brevity, we arbitrarily set $\gamma_0 = 0$ since it is just a scalar shift of energy spectrum and the parameters C_0, C_1 and C_2 are all normalized by C_3 in Figure 6.

Supporting Information

The Supporting Information is available free of charge on the ACS Publications website at DOI: 10.1021/acsnano.***.

Device fabrication and characterization, conductivity evolution near Dirac point, calculations of magnetic field effect on the graphene-TI hybridization, MR data at Dirac point, and transport properties of a device with electrode contacts on TI (PDF).

The authors declare no competing financial interest.

ACKNOWLEDGMENTS

This work was supported by National Key Research and Development Program of China (Nos. 2016YFA0300802, 2013CB934600) and NSFC (No. 11234001).

REFERENCES

1. Kane, C. L.; Mele, E. J. Quantum Spin Hall Effect in Graphene. *Phys. Rev. Lett.* **2005**, *95*, 226801.
2. Weeks, C.; Hu, J.; Alicea, J.; Franz, M.; Wu, R. Engineering a Robust Quantum Spin Hall State in Graphene *via* Adatom Deposition. *Phys. Rev. X* **2011**, *1*, 021001.
3. Hu, J.; Alicea, J.; Wu, R.; Franz, M. Giant Topological Insulator Gap in Graphene with 5d Adatoms. *Phys. Rev. Lett.* **2012**, *109*, 266801.
4. Jiang, H.; Qiao, Z.; Liu, H.; Shi, J.; Niu, Q. Stabilizing Topological Phases in Graphene *via* Random Adsorption. *Phys. Rev. Lett.* **2012**, *109*, 116803.
5. Balakrishnan, J.; Koon, G. K. W.; Jaiswal, M.; Castro Neto, A. H.; Oezyilmaz, B. Colossal Enhancement of Spin-Orbit Coupling in Weakly Hydrogenated Graphene.

Nat. Phys. **2013**, *9*, 284-287.

6. Avsar, A.; Tan, J. Y.; Taychatanapat, T.; Balakrishnan, J.; Koon, G. K. W.; Yeo, Y.; Lahiri, J.; Carvalho, A.; Rodin, A. S.; O'Farrell, E. C. T. Spin-Orbit Proximity Effect in Graphene. *Nat. Commun.* **2014**, *5*, 4875.
7. Wang, Z.; Ki, D.–K.; Chen, H.; Berger, H.; MacDonald, A. H.; Morpurgo, A. F. Strong Interface-Induced Spin-Orbit Interaction in Graphene on WS_2. *Nat. Commun.* **2015**, *6*, 8339.
8. Kaloni, T. P.; Kou, L.; Frauenheim, T.; Schwingenschlögl, U. Quantum Spin Hall States in Graphene Interacting with WS_2 or WSe_2. *Appl. Phys. Lett.* **2014**, *105*, 233112.
9. Kou, L.; Hu, F.; Yan, B.; Wehling, T.; Felser, C.; Frauenheim, T.; Chen, C. Proximity Enhanced Quantum Spin Hall State in Graphene. *Carbon* **2015**, *87*, 418–23.
10. Kou, L.; Yan, B.; Hu, F.; Wu, S.-C.; Wehling, T. O.; Felser, C.; Chen, C.; Frauenheim, T. Graphene-Based Topological Insulator with an Intrinsic Bulk Band Gap above Room Temperature. *Nano Lett.* **2013**, *13*, 6251-6255.
11. Jin, K. H.; Jhi, S. H. Proximity-Induced Giant Spin-Orbit Interaction in Epitaxial Graphene on a Topological Insulator. *Phys. Rev. B* **2013**, *87*, 075442.
12. Zhang, J.; Triola, C.; Rossi, E. Proximity Effect in Graphene-Topological-Insulator Heterostructures. *Phys. Rev. Lett.* **2014**, *112*, 096802.
13. Cao, W.; Zhang, R.-X.; Tang, P.; Yang, G.; Sofo, J.; Duan, W.; Liu, C.-X. Heavy

Dirac Fermions in a Graphene/Topological Insulator Hetero-Junction. *2D Mater.* **2016**, *3,* 034006.

14. Novoselov, K. S.; Geim, A. K.; Morozov, S. V.; Jiang, D.; Katsnelson, M. I.; Grigorieva, I. V.; Dubonos, S. V.; Firsov, A. A. Two-Dimensional Gas of Massless Dirac Fermions in Graphene. *Nature* **2005**, *438*, 197-200.
15. Zhang, Y.; Tan, Y. W.; Stormer, H. L.; Kim, P. Experimental Observation of the Quantum Hall Effect and Berry's Phase in Graphene. *Nature* **2005**, *438*, 201-204.
16. Hasan, M. Z.; Kane, C. L. Colloquium: Topological Insulators. *Rev. Mod. Phys.* **2010**, *82*, 3045.
17. Qi, X.-L.; Zhang, S.-C. Topological Insulators and Superconductors. *Rev. Mod. Phys.* **2011**, *83*, 1057.
18. Pesin, D.; Macdonald, A. H. Spintronics and Pseudospintronics in Graphene and Topological Insulators. *Nat. Mater.* **2012**, *11*, 409-416.
19. Lee, P.; Jin, K.-H.; Sung, S. J.; Kim, J. G.; Ryu, M.-T.; Park, H.-M.; Jhi, S.-H.; Kim, N.; Kim, Y.; Yu, S. U.; Kim, K. S.; Noh, D. Y.; Chung, J. Proximity Effect Induced Electronic Properties of Graphene on Bi_2Te_2Se. *ACS Nano* **2015**, *9*, 10861-10866.
20. Qiao, Z.; Ren, W.; Chen, H.; Bellaiche, L.; Zhang, Z.; Macdonald, A. H.; Niu, Q. Quantum Anomalous Hall Effect in Graphene Proximity Coupled to an Antiferromagnetic Insulator. *Phys. Rev. Lett.* **2014**, *112*, 116404.
21. Wei, P.; Lee, S.; Lemaitre, F.; Pinel, L.; Cutaia, D.; Cha, W.; Katmis, F.; Zhu, Y.; Heiman, D.; Hone, J.; Moodera, J. S.; Chen, C.-T. Strong Interfacial Exchange

Field in the Graphene/EuS Heterostructure. *Nat. Mater.* **2016**, *15*, 711.

22. Shoman, T.; Takayama, A.; Sato, T.; Souma, S.; Takahashi, T.; Oguchi, T.; Segawa, K.; Ando, Y. Topological Proximity Effect in a Topological Insulator Hybrid. *Nat. Commun.* **2015**, *6*, 6547.
23. Kim, N.; Lee, P.; Kim, Y.; Kim, J. S.; Kim, Y.; Noh, D.; Yu, S.; Chung, J.; Kim, K. S. Persistent Topological Surface State at the Interface of Bi_2Se_3 Film Grown on Patterned Graphene. *ACS Nano* **2014**, *8*, 1154– 1160.
24. Zhang, L.; Yan, Y.; Wu, H.-C.; Yu, D.; Liao, Z.-M. Gate-Tunable Tunneling Resistance in Graphene/Topological Insulator Vertical Junctions. *ACS Nano* **2016**, 10, 3816-3822.
25. Steinberg, H.; Orona, L. A.; Fatemi, V.; Sanchez-Yamagishi, J. D.; Watanabe, K.; Taniguchi, T.; Jarillo-Herrero P. Tunneling in Graphene–Topological Insulator Hybrid Devices. *Phys. Rev. B* **2015**, *92*, 241409.
26. Vaklinova, K.; Hoyer, A.; Burghard, M.; Kern, K. Current-Induced Spin Polarization in Topological Insulator-Graphene Heterostructures. *Nano Lett.* **2016**, *16*, 2595-2602.
27. Yan, Y.; Liao, Z.-M.; Ke, X.; Tendeloo, G. V.; Wang, Q.; Sun, D.; Yao, W.; Zhou, S.; Zhang, L.; Wu, H.-C.; Yu, D. P. Topological Surface State Enhanced Photothermoelectric Effect in Bi_2Se_3 Nanoribbons. *Nano Lett.* **2014**, *14*, 4389–4394.
28. Xia, Y.; Qian, D.; Hsieh, D.; Wray, L.; Pal, A.; Lin, H.; Bansil, A.; Grauer, D.; Hor, Y. S.; Cava, R. J.; Hasan, M. Z. Observation of a Large-Gap Topological-Insulator

Class with a Single Dirac Cone on the Surface. *Nat. Phys.* **2009**, *5*, 398– 402.

29. Fu, L. Hexagonal Warping Effects in the Surface States of the Topological Insulator Bi_2Te_3. *Phys. Rev. Lett.* 103, 266801 (2009).
30. Kuroda, K.; Arita, M.; Miyamoto, K.; Ye, M.; Jiang, J.; Kimura, A.; Krasovskii, E. E.; Chulkov, E. V.; Iwasawa, H.; Okuda, T.; Shimada, K.; Ueda, Y.; Namatame, H.; Taniguchi, M. Hexagonally Deformed Fermi Surface of the 3D Topological Insulator Bi_2Se_3. *Phys. Rev. Lett.* **2010**, *105*, 076802.
31. Wang, Y.; Deorani, P.; Banerjee, K.; Koirala, N.; Brahlek, M.; Oh, S.; Yang, H. Topological Surface States Originated Spin-Orbit Torques in Bi_2Se_3. *Phys. Rev. Lett.* **2015**, *114*, 257202.
32. Hwang, E.; Adam, S.; Sarma, S. D. Carrier Transport in Two-Dimensional Graphene Layers. *Phys. Rev. Lett.* **2007**, *98*, 186806.
33. Adam, S.; Hwang, E.; Galitski, V.; Sarma, S. D. A Self-Consistent Theory for Graphene Transport. *Proc. Natl Acad. Sci. USA* **2007**, *104*, 18392-18397.
34. Parish, M.; Littlewood, P. Non-Saturating Magnetoresistance in Heavily Disordered Semiconductors. *Nature* **2003**, *426*, 162-165.
35. Tiwari, R. P.; Stroud, D. Model for the Magnetoresistance and Hall Coefficient of Inhomogeneous Graphene. *Phys. Rev. B* **2009**, *79*, 165408.
36. Cho, S.; Fuhrer, M. S. Charge Transport and Inhomogeneity near the Minimum Conductivity Point in Graphene. *Phys. Rev. B* 77, 081402 (2008).

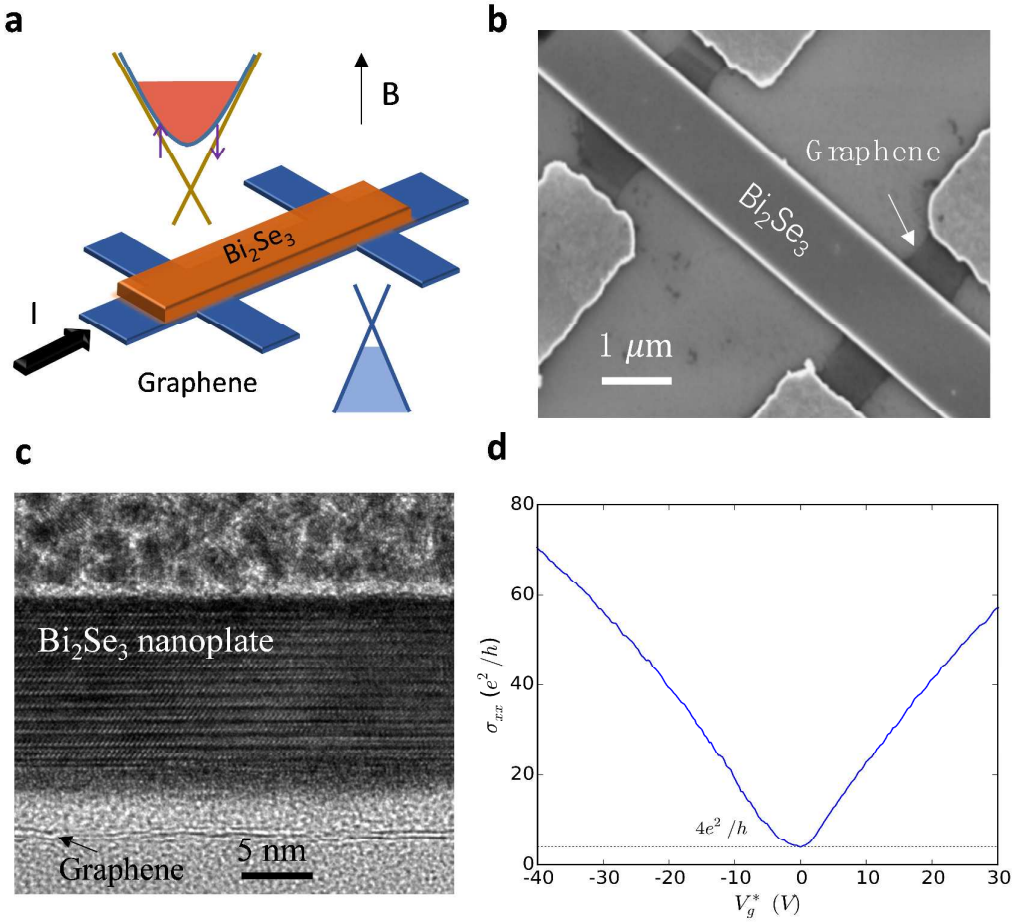

Figure 1. Characterizations of the device. (**a**) Schematic diagram of the hybrid device and the band structures of graphene and Bi_2Se_3. (**b**) SEM image of a typical device. (**c**) HRTEM image of a cross section from a typical graphene-Bi_2Se_3 heterostructure, where the graphene layer, Bi_2Se_3 quintuple layers and the thin oxide layer are indicated. (**d**) The gate voltage dependence of conductivity at 1.4 K. The position of the Dirac point has been shifted to zero volt.

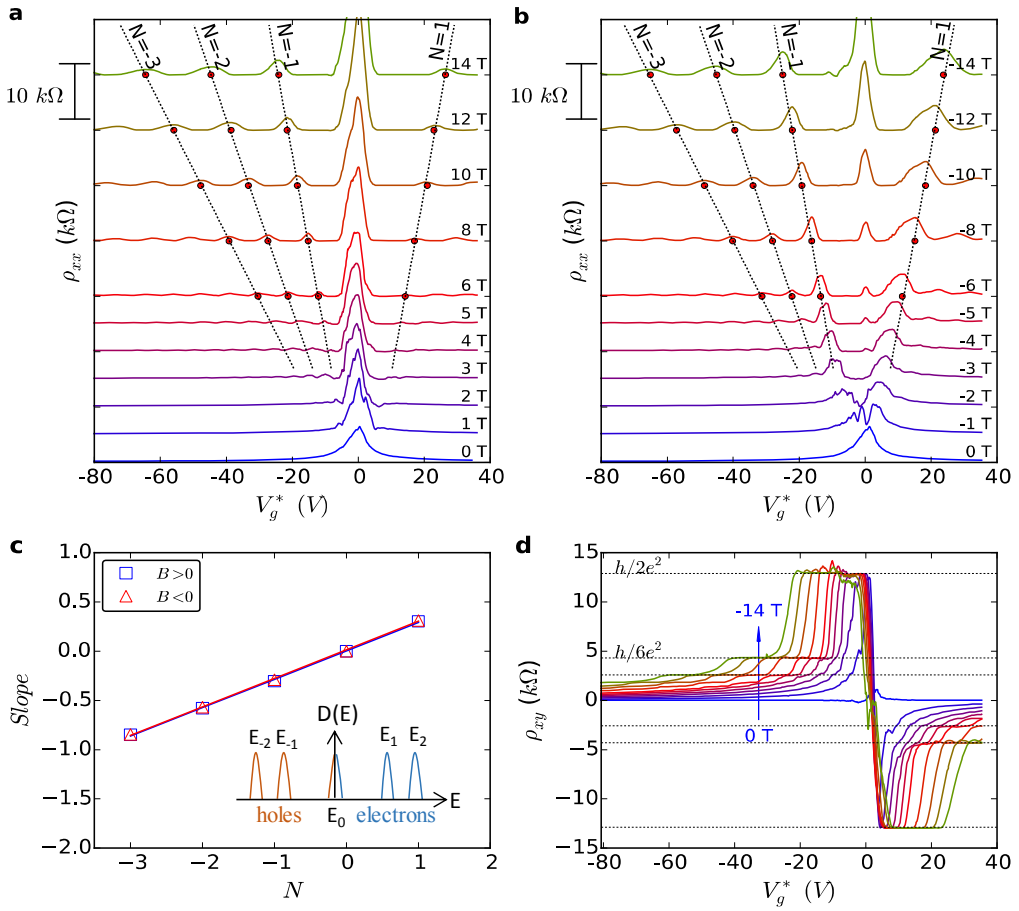

Figure 2. Magnetotransport at 1.4 K. The longitudinal resistivity ρ_{xx} *versus* gate voltage V_g^* in various (**a**) positive and (**b**) negative magnetic fields. The curves are shifted proportional to the magnetic field strength. The red filled circles indicate the positions $V_g^{*,p}$ of ρ_{xx} peaks. Dashed lines are linear fitting results, demonstrating the $V_g^{*,p} \propto B$. (**c**) The extracted slopes of the dashed lines in Figure 2a,b *versus* the Landau index *N*. The data can be linearly fitted. **(d)** The Hall resistivity ρ_{xy} as a function of V_g^* under negative magnetic fields corresponding to Figure 2b.

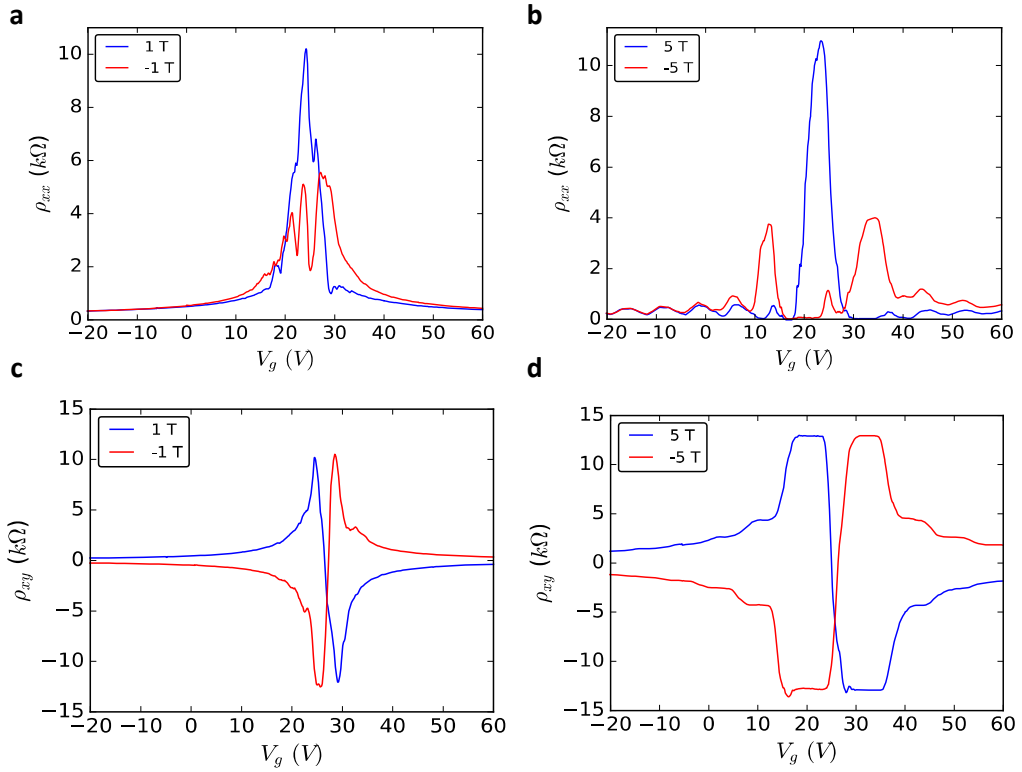

Figure 3. Hall measurements under both positive and negative magnetic fields. The longitudinal resistivity ρ_{xx} and Hall resistivity ρ_{xy} as a function of gate voltage V_g under various magnetic fields B at 1.4 K. The comparisons between $\rho_{xx}(V_g, B < 0)$ and $\rho_{xx}(V_g, B > 0)$ directly show the unusual graphene-topological insulator coupling effect.

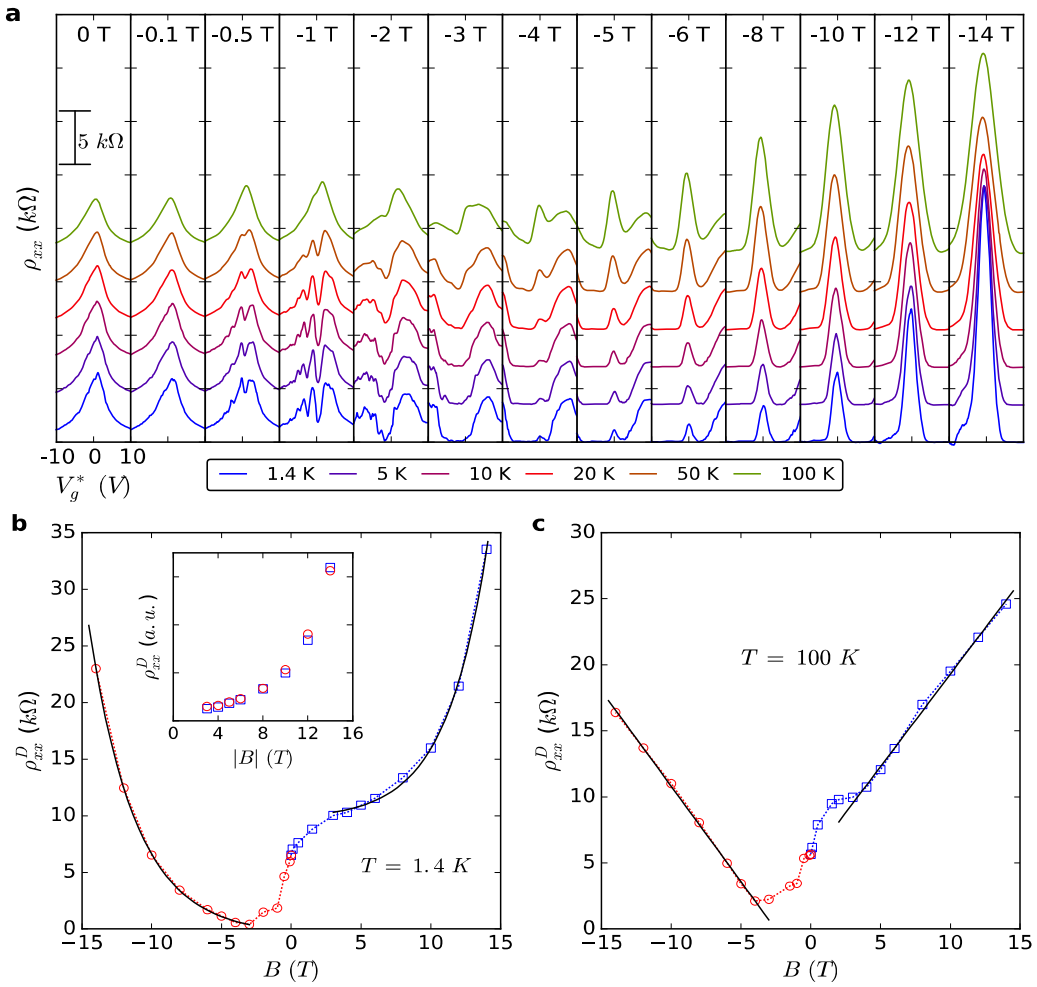

Figure 4. Resistance near the Dirac point. (**a**) The evolution of the V_g^* dependence of ρ_{xx} at various temperatures and negative magnetic fields. Curves are shifted in each panel for clarity. (**b**) The longitudinal resistivity at the Dirac point ρ_{xx}^{D} *versus* magnetic field B at 1.4 K. The solid curves show the exponential fitting as $|\mathrm{B}| \geq 3$ T. The ρ_{xx}^{D} *vs.* B has the same exponential factor for both positive and negative magnetic fields, as demonstrated in the inset, where the $\rho_{xx}^{\mathrm{D}}(B<0)$ data points (open red circles) are shifted up. (**c**) The ρ_{xx}^{D} *vs.* B at 100 K. The solid lines show the linear fitting results. The inset shows the ρ_{xx}^{D} *vs.* B at 10 K.

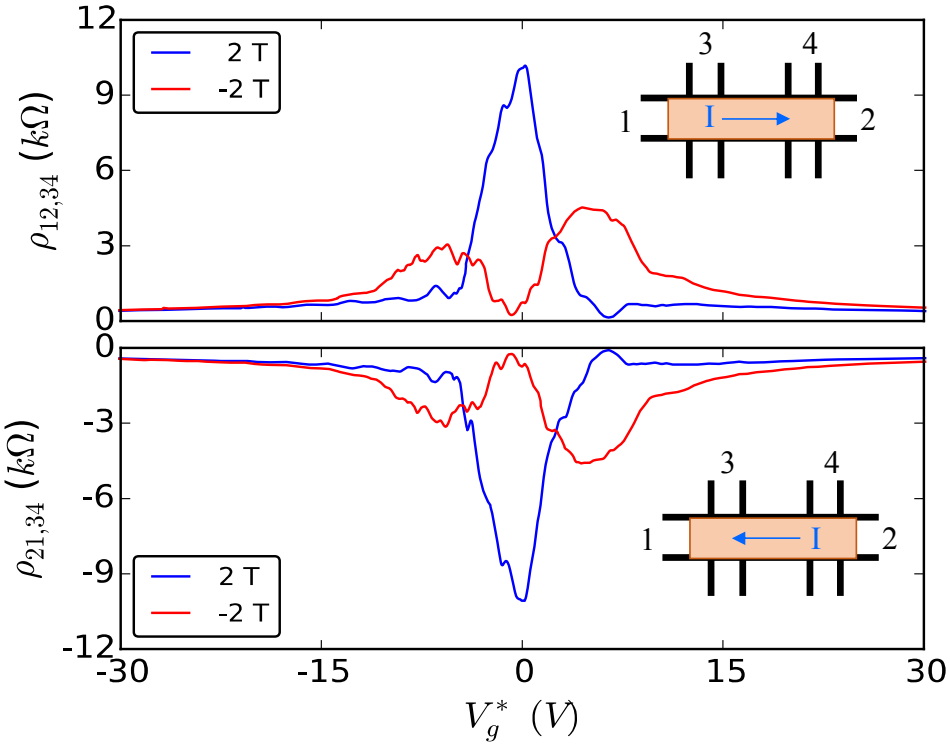

Figure 5. Longitudinal resistivity upon different directions of magnetic field and bias current. The gate voltage dependence of longitudinal resistivity under reversed direction of magnetic field (B = 2 and -2 T) and current (I = 0.1 and -0.1 μA) at 5 K excludes the Hall origin for the unconventional magnetotransport behaviors. The $\rho_{mn,kl}$ is defined as $\frac{W}{L}\frac{V_{kl}}{I_{mn}}$, where W is the width and L is the length of the Hall bar.

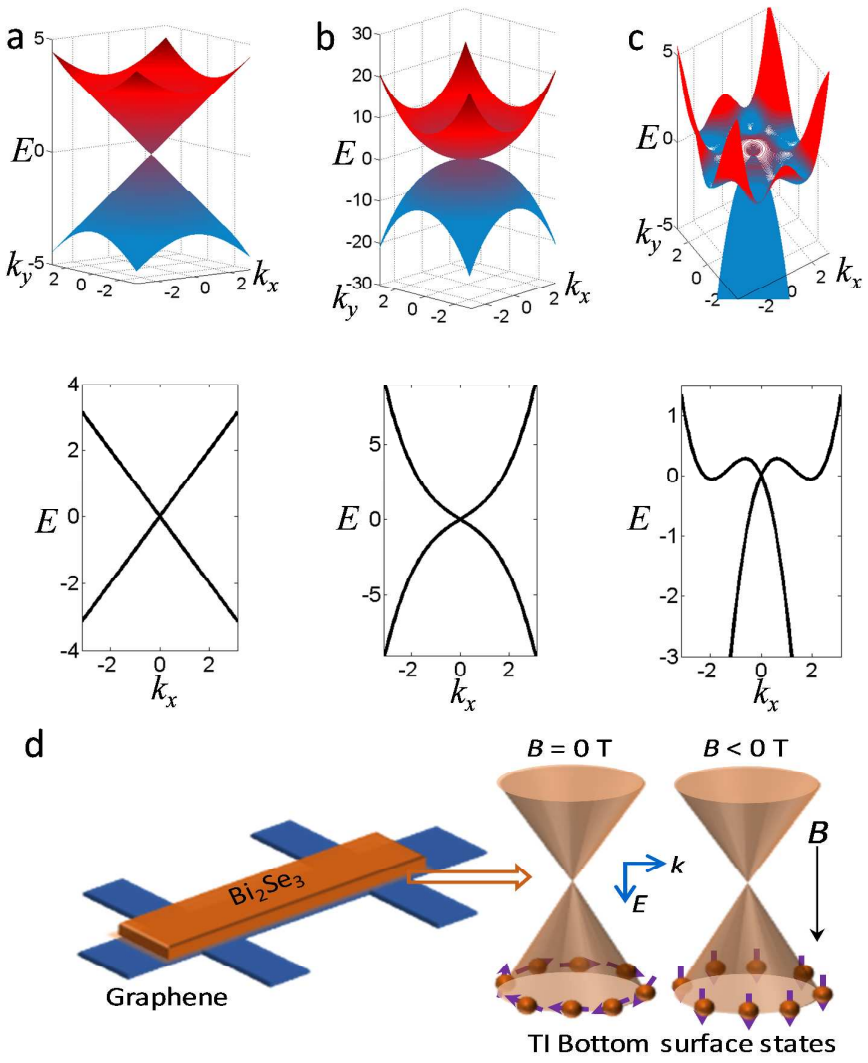

Figure 6. Schematic band structures of graphene hybridized with topological insulator bottom surface states according to the first-principle calculations and Hamiltonians in Eq (1). The Dirac like linear band in (**a**) is obtained from pristine graphene, *i.e.*, C_3=1, C_0=C_1=C_2=0. The nonlinear band in (**b**) is obtained by using C_0=C_1=0, C_2=0.2, and C_3=1. An oscillatory band structure is obtained in (**c**) by using C_0=C_3=1 and C_2=C_1=0.2. (**d**) Schematic bottom surface states of TI Bi_2Se_3 without and with negative magnetic field.

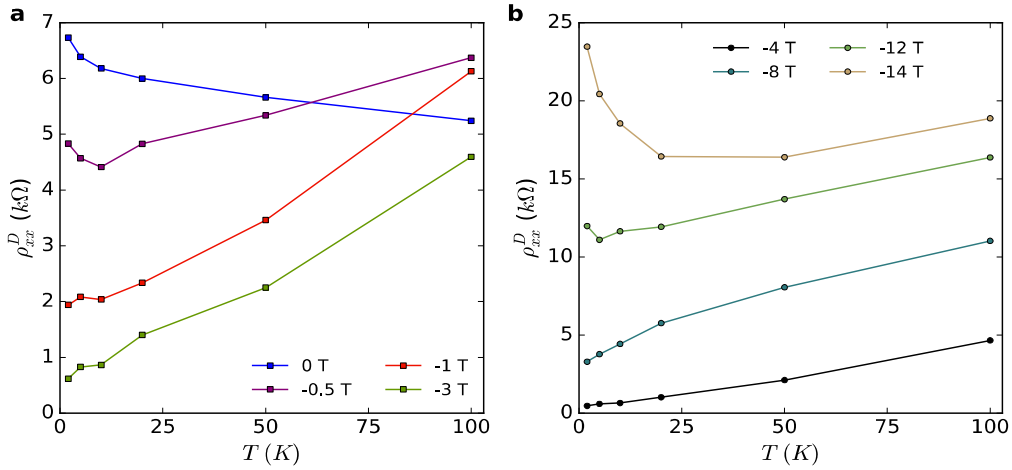

Figure 7. The longitudinal resistivity at the Dirac point ρ_{xx}^{D} *versus* temperature T at different magnetic fields.

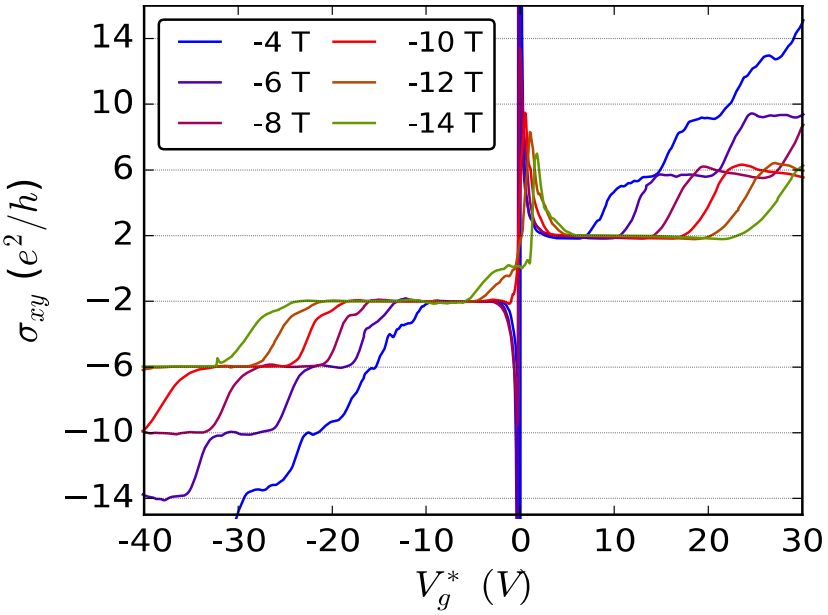

Figure 8. Hall conductivity at 1.4 K. The Hall conductivity σ_{xy} ($\sigma_{xy} = \rho_{xy}/(\rho_{xx}^2 + \rho_{xy}^2)$) as a function of V_g^* at different negative magnetic fields. The unconventional sharp conductivity peaks around the Dirac point arise from the longitudinal resistivity dips at the Dirac point. The deviation from strictly quantized conductivity in the electron branch is attributed to the scattering between the quantum Hall states and the conductive Bi_2Se_3 channel.

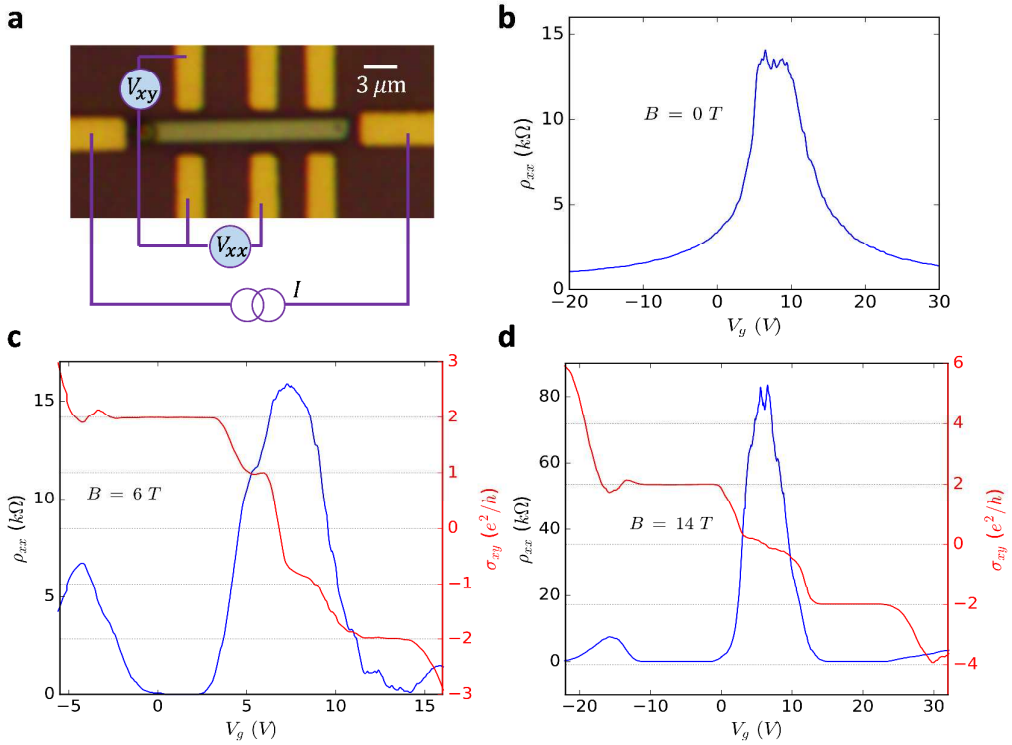

Figure 9. Transport of another graphene-Bi_2Se_3 hybrid device at 1.4 K. (**a**) The setup of Hall measurements. The channel length L is $4.5\ \mu m$ and the width W is $1.9\mu m$. (**b**) Longitudinal resistivity ρ_{xx} *versus* back gate voltage V_g without magnetic field. (**c, d**) ρ_{xx} and Hall conductivity σ_{xy} as a function of V_g under (**c**) 6 T and (**d**) 14 T. The Dirac point of this sample locates at ~7 V. The developing $\pm e^2/h$ Hall conductivity plateaus in (**c**) are observed, which may be sensitive to the graphene- Bi_2Se_3 coupling strength. Under higher magnetic field 14 T, zero Hall plateau at the Dirac point emerges in **(d)**, while such strong magnetic field ruins the coupling-induced fine structures in **(c).**